2000; Marthaler, 2003; Thomson and Mackay, 2004]. However, the Japanese public health policy has not employed these systems. In addition, only 58.9% of Japanese 3-year-old children use fluoride dentifrice [Japanese Society for Dental Health, 2003]. Therefore, in order to reduce dental caries disparities, an effective population strategy such as water or salt fluoridation might be required in Japan.

In conclusion, the effect of a topical fluoride application service of a municipality on caries prevalence in 3-year-old children has been shown to be statistically significant, though the clinical effect is less than the effect of sociodemographic characteristics.

Acknowledgment

We thank Kunihiko Takahashi for statistical advice.

References

Amstutz RD, Rozier RG: Community risk indicators for dental caries in school children: an ecologic study. Community Dent Oral Epidemiol 1995;23:129–137.

Antunes JLF, Frazao P, Narvai PC, Bispo CM, Pegoretti T: Spatial analysis to identify differentials in dental needs by area-based measures. Community Dent Oral Epidemiol 2002;30:133–142.

Benach J, Yasui Y, Borrell C, Rosa E, Pasarin MI, Benach N, Espanol E, Martinez JM, Daponte A: Examining geographic patterns of mortality: the atlas of mortality in small areas in Spain (1987–1995). Eur J Public Health 2003; 13:115–123.

Blair Y, Macpherson LM, McCall DR, McMahon AD, Stephen KW: Glasgow nursery-based caries experience, before and after a community development-based oral health programme's implementation. Community Dent Health 2004;21:291–298.

Daly B, Watt R, Batchelor P, Treasure E: Essential Dental Public Health. New York, Oxford University Press, 2003.

Dental Health Division of Health Policy Bureau, Ministry of Health, Labour and Welfare, Japan: Report on the Survey of Dental Diseases 1999. Tokyo, Oral Health Association, 2001.

8020 Promotion Foundation: Community Dental Health Data Bank. Tokyo. http://www.8020zaidan.or.jp/databank/index_chiiki.html, 2004.

Elliott P, Cuzick J, English D, Stern R: Geographical and Environmental Epidemiology. Oxford, Oxford University Press, 1997.

Ghosh M, Rao JNK: Small area estimation: an appraisal. Stat Sci 1994;9:55–76.

Japan Marketing Education Center: Individual Income Indices. Tokyo, Japan Marketing Education Center, 1999.

Japanese Society for Dental Health: Report of fluoride applications. J Dent Health 2003;53: 611–614.

Leroux BG, Maynard RJ, Domoto P, Zhu C, Milgrom P: The estimation of caries prevalence in small areas. J Dent Res 1996;75:1947–1956.

Marinho VCC, Higgins JPT, Logan S, Sheiham A: Fluoride varnishes for preventing dental caries in children and adolescents (review). Cochrane Database Syst Rev 2002;3: CD002279.

Marthaler TM: Successes and drawbacks in the caries-preventive use of fluorides: lessons to be learnt from history. Oral Health Prev Dent 2003;1:129–140.

Marthaler TM: Changes in dental caries 1953–2003. Caries Res 2004;38:173–181.

McDonagh MS, Whiting PF, Wilson PM, Sutton AJ, Chestnutt I, Cooper J, Misso K, Bradley M, Treasure E, Kleijnen J: Systematic review of water fluoridation. BMJ 2000;321:855–859.

Nadanovsky P, Sheiham A: Relative contribution of dental services to the changes in caries levels of 12-year-old children in 18 industrialized countries in the 1970s and early 1980s. Community Dent Oral Epidemiol 1995;23:331–339.

Riley JC, Lennon MA, Ellwood RP: The effect of water fluoridation and social inequalities on dental caries in 5-year-old children. Int J Epidemiol 1999;28:300–305.

Statistics and Information Department of Minister's Secretariat, Ministry of Health, Labour and Welfare: Report on Public Health Center Activities and Health Services for the Aged 2000. Tokyo, Health and Welfare Statistics Association, 2002a.

Statistics and Information Department of Minister's Secretariat, Ministry of Health, Labour and Welfare: Number of dentists: Survey on Physicians, Dentists and Pharmacists 2000. Tokyo, Health and Welfare Statistics Association, 2002b.

Statistics and Information Department of Minister's Secretariat, Ministry of Health, Labour and Welfare: Vital Statistics of Japan 2000. Tokyo, Health and Welfare Statistics Association, 2002c.

Statistics Bureau, Ministry of Internal Affairs and Communications: 2000 Population Census. Tokyo, Statistical Information Institute for Consulting and Analysis, 2002.

Takahashi K: EB estimator for Binomial-Beta model. Saitama. http://www.niph.go.jp/soshiki/gijutsu/download/, 2004.

Tango T: Disease mapping and spatial disease clustering: toward an appropriate interpretation and use of disease indices. J Natl Inst Public Health 1999;48:84–93.

Thomson WM, Mackay TD: Child dental caries patterns described using a combination of area-based and household-based socio-economic status measures. Community Dent Health 2004;21:285–290.

Truin GJ, van Rijkom HM, Mulder J, van't Hof MA: Caries trends 1996–2002 among 6- and 12-year-old children and erosive wear prevalence among 12-year-old children in The Hague. Caries Res 2005;39:2–8.

Vanobbergen J, Declerck D, Mwalili S, Martens L: The effectiveness of a 6-year oral health education programme for primary schoolchildren. Community Dent Oral Epidemiol 2004;32:173–182.

Watt R, Sheiham A: Inequalities in oral health: a review of the evidence and recommendations for action. Br Dent J 1999;187:6–12.

Yiannakoulias N, Rowe BH, Svenson LW, Schopflocher DP, Kelly K, Voaklander DC: Zones of prevention: the geography of fall injuries in the elderly. Soc Sci Med 2003;57:2065–2073.

Yu XQ, O'Connell DL, Gibberd RW, Smith DP, Dickman PW, Armstrong BK: Estimating regional variation in cancer survival: a tool for improving cancer care. Cancer Causes Control 2004;15:611–618.

Available online at www.sciencedirect.com
SCIENCE DIRECT®
Journal of Non-Crystalline Solids 352 (2006) 2628–2630
JOURNAL OF NON-CRYSTALLINE SOLIDS
www.elsevier.com/locate/jnoncrysol

Photochemical fabrication of molecular devices

Toshio Naito [a,b,*], Hideyuki Sugawara [b], Tamotsu Inabe [b], Takeshi Miyamoto [c], Hironobu Niimi [c,d], Kiyotaka Asakura [c]

[a] *Department of Creative Research Initiative 'Sousei' (CRIS), Hokkaido University, Kita 21, Nishi 10, Kita-ku, Sapporo, Hokkaido 001-0021, Japan*
[b] *Division of Chemistry, Graduate School of Science, Hokkaido University, Kita 10, Nishi 8, Kita-ku, Sapporo, Hokkaido 060-0810, Japan*
[c] *Catalysis Research Center (CRC), Hokkaido University, Kita 21, Nishi 10, Kita-ku, Sapporo, Hokkaido 001-0021, Japan*
[d] *CREST-JST*

Available online 24 May 2006

Abstract

We present a novel way to fabricate electronic devices from a molecular charge transfer salt $Ag(DM)_2$ by simple illumination, which realizes a junction-structure in the single molecular crystal. The electrical conductivity of the selected parts of samples can be controlled by illimination time and power. The electrical behavior gradually turned semiconducting from metallic one by illumination. X-ray photoelectron spectroscopy, Raman spectroscopy and X-ray absorption fine structure indicated that illumination should transfer some electrons from the conducting DM columns to the Ag ions. The X-ray powder diffraction pattern indicated that original crystal lattice was maintained after the illumination. These observations imply that the illumination practically effected *doping* (or rather *dedoping*) on the material.

PACS: 73.40.Ei; 73.40.Ns

Keywords: Oxidation reduction; Electrical and electronic properties; Band structure; Conductivity; Optical spectroscopy; Photoinduced effects; XPS

1. Introduction

A large number of molecular conductors have been reported to date [1–5]. Most of them contain planar π-conjugated molecules with multi-redox reactivities, which exist as metastable partially charged radical-ions in the conducting solids. In general, their electrical conduction is supported by the unpaired electrons delocalized through π-bands, i.e., overlaps of the π-molecular orbitals among adjacent molecular radical-ions. They usually have structurally unique and various conduction pathways such as columns, sheets, ladders and spirals, depending on the structures and arrangements of constituent molecular species. Some of them also contain photosensitive chemical species such as silver ions and bypyridyl derivatives, which are not involved in the conduction pathways. Such solids are generally stable in ambient conditions. However, they could be reactive under illumination of ultraviolet and visible (UV–VIS) light, where electron transfer could occur between the photosensitive and the molecular species responsible for the conduction. As a result, illumination could irreversibly increase or decrease the amount of conduction electrons by their addition or removal. In combination with photolithography or light-focusing technique, this might open a new way to control irreversibly electrical properties of a particular part of a molecular solid, which would lead to fabrication of devices with junction-strutures. In this paper, we present an optical

* Corresponding author. Address: Department of Creative Research Initiative 'Sousei' (CRIS), Hokkaido University, Kita 21, Nishi 10, Kita-ku, Sapporo, Hokkaido 001-0021, Japan. Tel./fax: +81 11 706 9213.
E-mail address: tnaito@mail.cris.hokudai.ac.jp (T. Naito).

0022-3093/$ - see front matter © 2006 Elsevier B.V. All rights reserved.
doi:10.1016/j.jnoncrysol.2006.01.097

control method of electrical properties of molecular solids together with its mechanism.

2. Experimental

The silver salt of dimethyl-dicyanoquinonediimine (DM), $Ag(DM)_2$, was prepared according to [6]. The electrical resistivity measurements were carried out using a standard 4-probe method with gold wires and gold paste as electrical contacts. A part of the sample (a single crystal or a pressed pellet) or the whole sample was continuously illuminated with UV–VIS light (200–1100 nm) using an optical fiber. Subsequently, the physical measurements were carried out for the sample using conventional procedures in the dark. Parallel measurements of the pristine samples were also conducted for checking out any artefacts. After the measurements, the illumination was recommenced on the same sample and further illumination effects were investigated. The details of illuminations and measurements of physical and spectroscopic properties were described in earlier papers [7–9].

3. Results and discussion

DM forms charge transfer salts with various kinds of metals [6]. Owing to its moderate electron accepting ability, the DM molecules usually exist as radical anions with fractional valency in these salts. In the crystal of $Ag(DM)_2$, the planar radical anions of DM stack to form a columnar structure (Fig. 1). The unpaired electrons on the radical anions delocalize along these columns, resulting in metallic conduction. All the DM anions are coordinated to the Ag ions through the =N—CN groups at both ends of the fully π-conjugation system on the molecule. It was observed that $Ag(DM)_2$ qualitatively altered its electrical properties after illumination with wavelengths of 200–1100 nm: the temperature-dependence of a partially illuminated single crystal of $Ag(DM)_2$ was qualitatively explained as a sum of the electrical behavior of the illuminated and the non-illuminated parts of the sample (Fig. 2) [8]. In the range of 200–1100 nm, wavelength-dependence was not observed. The duration of illumination required for the change of physical properties varied from a few minutes to a few weeks depending mainly on the power of the light and the temperature.

Firstly, let us discuss what is happening in the sample during illumination. In the previous paper [8] we reported that X-ray photoelectron spectroscopy (XPS) was powerful tool to determine the chemical states of the illuminated part of the sample as well as how clear the borderline between the illuminated and the pristine parts of the sample was. The high-resolution XPS demonstrated that bulk silver (Ag(0)) was detected exclusively in the illuminated area while silver(I) (Ag(I)) ions remained unaffected in the non-illuminated area. In addition, the borderline was so sharp and clear that Ag(0) was not detected even in adjacent parts of the illuminated area. If the charge (electron)

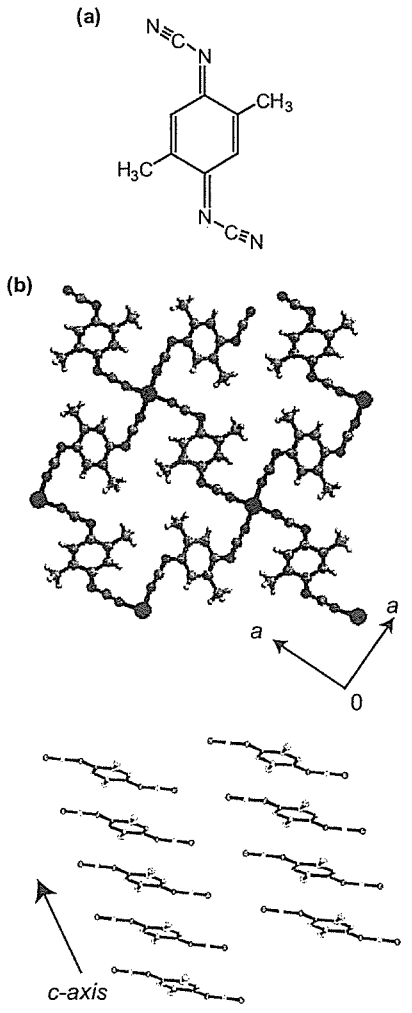

Fig. 1. (a) Molecular structure of DM and (b) crystal structure of $Ag(DM)_2$.

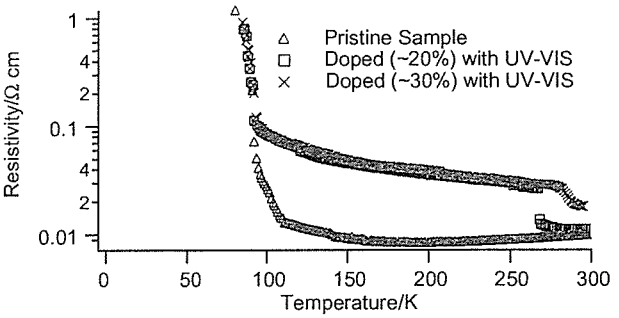

Fig. 2. UV–VIS illumination effects on the temperature-dependence of the electrical resistivity of an $Ag(DM)_2$ single crystal.

transfer actually occurred between the Ag and the DM ions, the XPS of the atoms in the DM ions should be consistent with the XPS of silver atoms. In fact, the XPS of nitrogen atoms in the illuminated sample clearly indicated that the DM radical anions were oxidized toward neutral DM molecules (Fig. 3). Since XPS is surface-sensitive, we

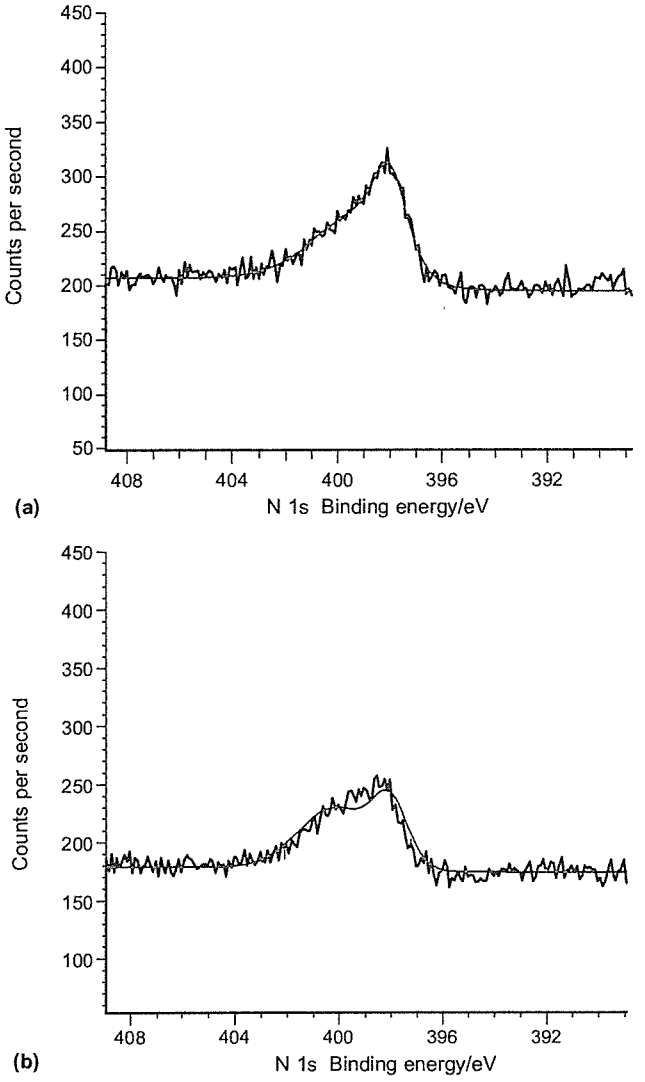

Fig. 3. N1S XPS of (a) pristine, and (b) illuminated samples. Note that a shoulder at lower energy appears more clearly in the illuminated sample, which can be attributed to the increase of the contribution from formally neutral DM molecules.

measured X-ray absorption fine structure (XAFS) in order to obtain information on the bulk of the samples. Along with the results of infrared spectra and elemental analyses, XAFS and XPS are consistently explained supposing that the illumination progressively induced electron transfer (redox reaction) between the Ag(I) ions and the DM radical anions. The interpretation thus far is consistent with a series of Raman spectra measured continually during the illumination [8], which indicated the formal charge of the DM radical anions continuously changed from −0.5 to −0.35 to −0.40 in accordance with the UV–VIS illumination. Identical spectra were obtained several months after ceasing illumination, which means the photochemically induced state as well as the interface between the illuminated and the non-illuminated areas are stable. Powder X-ray diffraction patterns proved that the illuminated samples retained the original (pristine) crystal structure. However, the apparent irreversibility of the phenomena suggests that there should be some difference between the structures before and after illumination. This issue is under investigation.

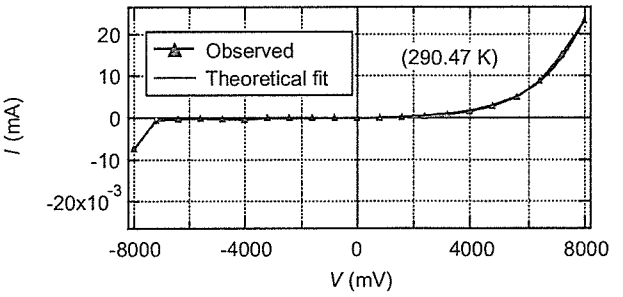

Fig. 4. *I–V* property curve of a single crystal of $Ag(DM)_2$ after UV–VIS illumination on the only half of it. The illumination continued for about three weeks from both sides of the needle crystal at room temperature.

It is highly possible that one could *dope* this material simply by illumination with virtually retaining the crystal structure. Thus we tried to make a rectifier from a single crystal of $Ag(DM)_2$ by illuminating on the only half of the long needle crystal. This was expected to remove some conduction electrons from the π-band of DM columns only in the illuminated part of the crystal, while leaving the rest of the crystal intact. Such partial photochemical treatment would force the crystal to take a junction-structure due to the imbalance of the Fermi levels at the interface. After illumination the *I–V* property curves were measured (Fig. 4). The result clearly shows that electric current exponentially increases when a forward voltage is applied, while it hardly flows when the applied voltage is reversed. Such 'one-way' conduction is called rectification, demonstrating its junction-structure and being characteristic to diodes. In other words, the illumination transformed a single crystal into a diode. This method was originally meant for the molecular crystals, yet it could be applicable to thin films and amorphous solids as well as inorganic materials.

References

[1] P. Batail (Ed.), Chem. Rev. 104 (2004), Thematic Issue for Molecular Conductors.
[2] J.-P. Farges (Ed.), Organic Conductors, Dekker, New York, 1994.
[3] H.S. Nalwa (Ed.), Handbook of Organic Conductive Molecules and Polymers, 1, Wiley, Stuttgart, 1997.
[4] J.M. Williams, J.R. Ferraro, R.J. Thorn, K.D. Carlson, U. Geiser, H.H. Wang, A.M. Kini, M.-H. Whangbo, The Physics and Chemistry of Organic Superconductors (Including Fullerenes), Prentice-Hall, Englewood Cliffs, NJ, 1992.
[5] T. Ishiguro, K. Yamaji, G. Saito, Organic Superconductors, second ed., Springer, New York, 1998.
[6] A. Aumüller, S. Hünig, Liebigs Ann. Chem. (1986) 142.
[7] T. Naito, T. Inabe, K. Takeda, K. Awaga, T. Akutagawa, T. Hasegawa, T. Nakamura, T. Kakiuchi, H. Sawa, T. Yamamoto, et al., J. Mater. Chem. 11 (2001) 2221.
[8] T. Naito, T. Inabe, H. Niimi, K. Asakura, Adv. Mater. 16 (2004) 1786.
[9] T. Naito, H. Sugawara, T. Inabe, T. Miyamoto, H. Niimi, K. Asakura, Mol. Cryst. Liq. Cryst., in press.

X-ray absorption fine structure (XAFS) analyses of Ni species trapped in graphene sheet of carbon nanofibers

Mayuko Ushiro, Kanae Uno, and Takashi Fujikawa*
Graduate School for Science, Chiba University, Yayoi-cho 1-33, Inage-ku, Chiba 263-8522, Japan

Yoshinori Sato and Kazuyuki Tohji
Graduate School of Environmental Studies, Tohoku University, Aoba, Sendai 980-8579, Japan

Fumio Watari
Graduate School of Dental Medicine, Department of Biomedical, Dental Materials and Engineering, Hokkaido University, Kita 13 Nishi 7, Sapporo, 060-8586, Japan

Wang-Jae Chun
Catalysis Research Center, Hokkaido University and Core Research for Evolution Science and Technology, Japan Science and Technology Corporation, Kita 21 Nishi 11, Sapporo, 001-0021, Japan

Yuichiro Koike and Kiyotaka Asakura
Catalysis Research Center, Department of Quantum Science and Engineering, Hokkaido University, Kita 21 Nishi 11, Sapporo, 001-0021, Japan

(Received 28 October 2005; revised manuscript received 28 December 2005; published 10 April 2006)

Metal impurities in the carbon nanotubes and carbon nanofibers play an important role in understanding their physical and chemical properties. We apply the Ni *K*-edge x-ray absorption fine structure analyses to the local electronic and geometric structures around embedded Ni impurities used as catalysts in a carbon nanofiber in combination with multiple scattering analyses. We find almost Ni catalysts as metal particles are removed by the purification treatment. Even after the purification, residual 100 ppm Ni species are still absorbed; most of them are in monomer structure with Ni-C bond length 1.83 Å, and each of them is substituted for a carbon atom in a graphene sheet.

DOI: 10.1103/PhysRevB.73.144103 PACS number(s): 61.10.Ht, 87.64.Fb, 87.64.Gb, 61.46.−w

I. INTRODUCTION

Carbon nanotubes (CNTs)[1,2] and carbon nanofibers (CNFs)[3,4] are promising nano materials for electric devices, hydrogen reservoir, reinforce composites, medical usages and so on. There are several preparation methods to produce CNTs/CNFs, where the metal catalysts play a decisive role in their production processes. Although most of them can be removed from the CNTs/CNFs by acid treatments,[5] a small amount of impurities are left in the CNTs/CNFs after the purification processes.[6] The metals are intimately associated with the nanotube samples.[6] These impurities are reported to affect a giant thermopower due to a Kondo effect,[7] quantum conductance,[8] and anomalous temperature dependence of the resistivity.[9] In addition to the modification of the physical properties of CNTs/CNFs some metals such as Ni show biotoxic effects on a human body when they are used in medical applications such as drag delivery systems, medical implants and scaffolds.[10–12] In order to understand the effect of metal atoms on the physical properties as well as the removal of these impurities, the structure of metal species left in the CNT will be important. Furthermore the knowledge about the local structure will provide a hint to the formation mechanism for the CNTs/CNFs.

From these standpoints of view the structures of metal species trapped in CNTs and CNFs have intensively been discussed theoretically. Several adsorption sites and model structures are proposed such as adsorption on Stone-Wales defects,[13] monomer or dimer adsorption model on the graphene sheet,[14] metal adsorption on atop of C atom[9,15] or on axial C-C bond,[16] a substitutional site of graphene sheet.[17,18] Lee *et al.* propose Ni-C σ bond is formed during the catalytic formation reaction of a single wall CNT and a Ni may be trapped at a substitutional position in the CNT wall.[19] However, we have had no definite conclusion for the location of metal atoms due to the lack of direct experimental evidence about the local structure around the metal impurities.

Recently Asakura *et al.* reported a letter concerning extended x-ray absorption fine structure (EXAFS) studies on the structure of Ni impurities left in a CNF after the purification.[20] Ni is one of the important catalyst to prepare CNTs and CNFs. They concluded that the dimer species were embedded in the CNFs with covalent Ni-C bonds. However, there are two criticisms on their conclusions.

(1) Where are these Ni atoms located?

(2) Are they really in dimers?

The first question comes from the fact that EXAFS is a one-dimensional local structure analysis sensitive to the short range order around the metal within about 3 Å. The second question arises based on the Ni-Ni distance 2.48 Å found in the EXAFS analysis, the distance is almost equal to that of Ni foil. The Ni-Ni bonds they observed could be due to those

of trace amount of Ni particles left after the purification.

X-ray absorption near edge structure (XANES) spectra provide longer range information (typically ≈5 Å) than EXAFS spectra, and stereochemical information.[21,22] Although XANES contains more information than EXAFS,[22] XANES analysis is difficult because it requires multiple scattering calculations. Hence, XANES has often been used as a fingerprint by comparing it with those of reference compounds. Fujikawa *et al.* have developed a reliable XANES theory based on the short range order full multiple scattering approach.[23] They have successfully determined several material structures by simulating XANES spectra.[24–28] Asakura *et al.* have measured the XANES spectra of these species and have observed prominent spectral features after the purification. The spectral features are different from those found in Ni foil or Ni oxide, and are characteristic of Ni species in CNFs after the purification treatment. The detailed XANES analyses will provide important information about the above criticisms.

In this paper we report x-ray absorption fine structure (XAFS) analyses on the local structures around Ni in a CNF. First we describe EXAFS analyses of the Ni residue involved in a CNF before and after the purification in details. Second we explain the XANES analyses and investigate plausible structures. We find Ni atoms substitute carbon atoms in the CNF framework. Finally we compare the present result with the previous theoretical works, and discuss the merits of XANES in the material science.

II. EXPERIMENT

CNF is synthesized by a CVD method using Ni catalyst following a previous literature.[29] The CNF used here is hat-stacked carbon nanofiber (HSCNF) that is composed of graphene hats stacked toward the needle axis.[12] The diameter and the length of the CNF is 25–100 nm and 0.1–5.0 μm, respectively. It is purified by a calcination in atmosphere followed by 6.0 M HCl treatment for 6 hours in order to remove the carbon nanoparticles and Ni catalysts.

XAFS measurements are carried out at the BL9A in the Institute for Structure Material Science's Photon Factory (KEK-PF) using a Si(111) double crystal monochromator (99G280, 2001G117, and 2003G2477). A pair of bent conical

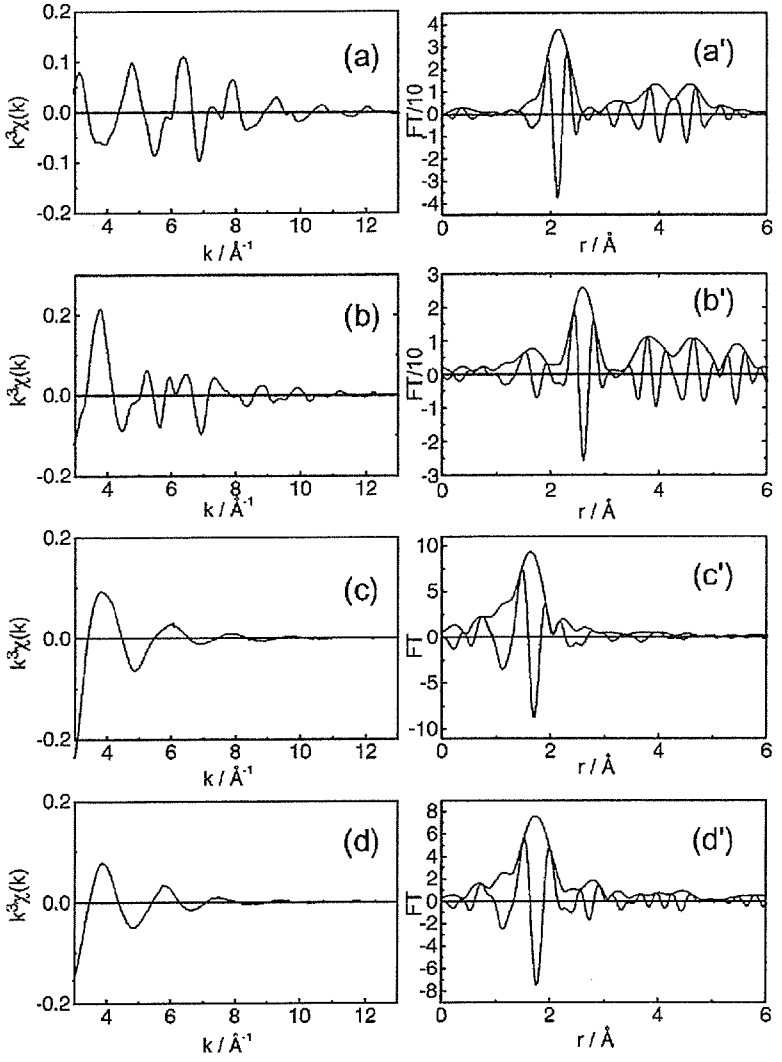

FIG. 1. Ni *K*-edge EXAFS oscillations (x) (x=a,b,c,d) and their Fourier transforms (x') (x'=a′,b′,c′,d′) of reference compounds: (a) (a′) Ni foil, (b) (b′) NiO, (c) (c′) $Ni(H_2O)_6(NO_3)_2$, and (d) (d′) $Ni(cp)_2$.

TABLE I. Curve fitting results for reference compounds. r is the distance to the neighbor, σ is the Debye-Waller factor, ΔE is a shift in edge energy, R is R-factor defined by Eq. (1), S is an amplitude reduction factor.

Sample	Bond	N	r/Å	$\sigma/10^{-2}$ Å	ΔE/eV	R/%	S
Ni foil	Ni-Ni	9.7±1.2 12[a]	2.47±0.02 2.49[a]	7.1±2.0	−11±5	1.0	0.80±0.1
NiO	Ni-O	5.8±0.4 6[a]	2.07±0.01 2.084[a]	8.0±1.0	−4.8±5	0.7	0.93±0.06 (Ref. 53)
	Ni-Ni	12.4±1.0 12[a]	2.95±0.02 2.954[a]	8.1±1.0	−3.5±3		1.0±0.1 (Ref. 53)
$Ni(H_2O)_6(NO_3)_2$	Ni-O	6.2±0.4 6[a]	2.04±0.01 2.063[a]	8.0±0.9	−2.0±1.0	3.5	1.0±0.1 (Ref. 54)
$Ni(C_5H_5)_2$	Ni-C	10.8±1.2 10[a]	2.17±0.01 2.196[a]	8.6±1.0	−5.7±3.0	3.0	1.1±0.1 (Ref. 55)

[a]The diffraction data.

mirrors focus the x-ray beam on the sample and remove higher harmonics.[30] The incident and transmitted x rays are monitored by ionization chambers filled with nitrogen. The fluorescence x rays are detected by a 19 element SSD (Solid State Detector, Camberra Co.). The dead times of SSD are corrected according to the literature.[31] The XAFS analyses are carried out by REX2000 (Rigaku Co.)[32,33] using phase shift and amplitude functions obtained from FEFF8.[21] The Fourier transformation of k^3-weighted $\chi(k)$ is carried out over the range $k=3-13$ Å^{-1}. The peaks are Fourier filtered with $\Delta r=1.2-2.2$ Å for the first shell with a Hamming window function, and the curve fitting analyses are carried out in the k-space. The goodness of fit is estimated by use of the R-factor defined by

$$R(\%)=\frac{\sum[k^3\chi_o(k)-k^3\chi_c(k)]^2}{\sum[k^3\chi_o(k)]^2}\times 100, \tag{1}$$

where χ_o and χ_c are the observed and the calculated fitting EXAFS oscillations.

III. THEORY

The XANES theory used in this paper is based on the short-range-order full multiple scattering theory proposed by Fujikawa *et al.*[34] Later, this theory was modified by a partitioning technique in order to reduce the computation time.[23,35–37] Here, we summarize the theoretical methods.

The x-ray absorption intensity σ from the core orbital $\phi_c(\mathbf{r})=R_{l_c}(r)Y_{L_c}(\hat{\mathbf{r}})$, $L_c=(l_c,m_c)$ at site A (x-ray absorbing atom) is given by Eq. (2) for photoelectron kinetic energy $\epsilon_k=k^2/2$. We assume excitation by a linearly polarized x ray in the z direction,[23]

$$\sigma=-\frac{8}{3}\mathrm{Im}\Bigg(\sum_{L,L',L_c} i^{l-l'}\exp[i(\delta_l^A+\delta_{l'}^A)]\rho_c(l)\rho_c(l') \times G(L_c10|L)G(L_c10|L')(t^{-1})_{LL}^{AA}[(1-X)^{-1}]_{LL'}^{AA}\Bigg), \tag{2}$$

where $G(LL'|L'')$ is Gaunt's integral and $\rho_c(l)$ is the radial dipole integral between the radial part of $\phi_c(\mathbf{r})$ and the lth partial wave of photoelectrons $R_l(r)$ at site A. The phase shift of the lth partial wave at site A is represented by δ_l^A. We introduce the matrix X specified with site index α and angular momentum L and so on; it is defined as

$$X_{LL'}^{\alpha\beta}=t_l^\alpha G_{LL'}(\mathbf{R}_\alpha-\mathbf{R}_\beta)(1-\delta_{\alpha\beta}), \tag{3}$$

where t_l^α and $G_{LL'}$ represent the T-matrix at site α and the Green's function in an angular momentum representation. The inverse matrix $(1-X)^{-1}$ includes an infinite order of the full multiple scattering inside the cluster we are considering. The phase shifts in $t_l^\alpha\{=-[\exp(2i\delta_l^\alpha)-1]/2ik\}$ are one of the most important features and reflect the electronic structure of the surrounding atoms, which are calculated within the Hartree-Fock approximation. The Green's function $G_{LL'}$ reflects the geometrical structure. The clusters used in the present work include all surrounding atoms up to about 5 Å for the carbide model and about 7 Å for other models around an x-ray absorption atom.

IV. RESULTS AND DISCUSSION

A. EXAFS

We measure the x-ray spectra of Ni foil, NiO, $Ni(H_2O)_6(NO_3)_2$, $Ni(cp)_2$ (cp=cyclopentadienyl), as reference compounds whose EXAFS oscillations and Fourier transforms are given in Fig. 1. We carry out curve fitting analyses to check the validity of FEFF calculations and to obtain the correction parameters, S, for coordination numbers. The results are summarized in Table I: The curve fitting analyses can provide 0.02 Å accuracy in the bond length. The coordination numbers are a little scattered but the reduction factor S can be determined within 10% precision. We obtain the averaged reduction factors $S=0.9\pm0.1$ for Ni-Ni, and $S=1.0\pm0.1$ for Ni-C and Ni-O.

Figure 2 shows the observed Ni K-edge EXAFS spectra, their Fourier transforms and curve fitting results of Ni in the CNFs before and after the purification. Before the purification, the EXAFS oscillation is found to be similar to that of

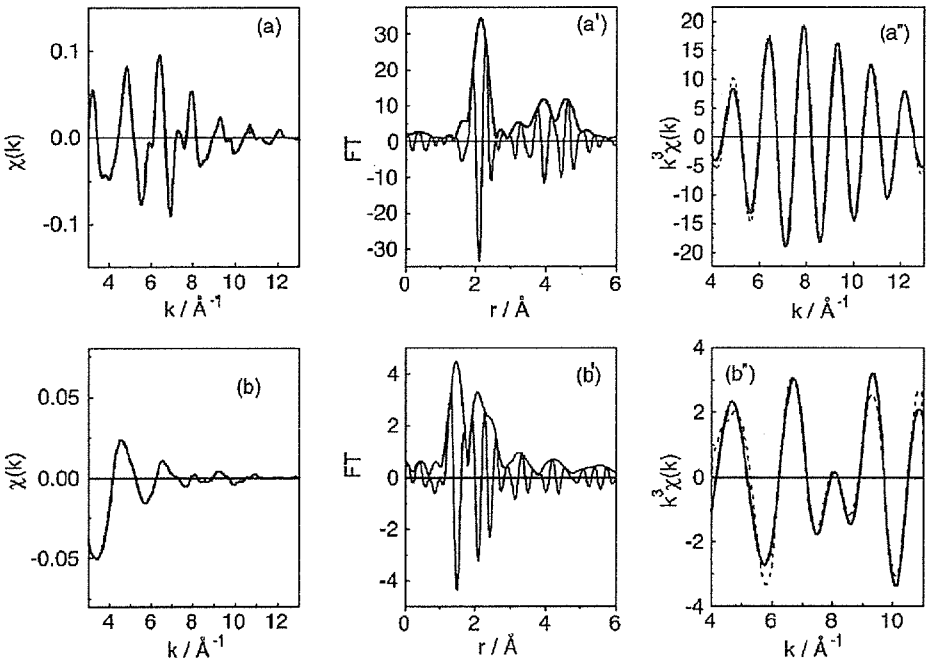

FIG. 2. (Color online) Ni *K*-edge EXAFS spectra (a,b), their Fourier transforms (a′,b′) and curve fitting results (a″,b″) before (a,a′,a″) and after the purification (b,b′,b″). In (a″) and (b″) the solid lines show the Fourier filtered EXAFS whereas the dashed lines show the fitted EXAFS.

Ni foil up to high k region; this result indicates the presence of Ni particles. Its Fourier transform has several peaks corresponding to those for Ni foil: Shape and pattern in 0–6 Å range are similar to those of the foil. The Ni particle size is estimated to be longer than 50 Å according to the Greegor's relationship between the size and the coordination numbers.[38] The result is consistent with the XRD and SEM data.[12] Table II shows the curve fitting results for the first shell of Ni in the CNF before purification. The coordination number is 10.8 after the reduction factor correction, which is slightly reduced from 12. This result may be caused by the intrinsic disorder in the Ni particles or the effect of impurity which is hardly observed in the EXAFS Fourier transform. As shown later, we still observe some deviation in the XANES spectrum before the purification from that of Ni foil, which indicate the presence of Ni-O bonding. We carry out two-shell fitting including Ni-O and Ni-Ni, and find better fitting results for the parameters listed in Table II, where R-factor 0.65% for the two-shell fitting is much smaller than 1.0% for the one shell fitting. The fitting EXAFS curve shows the excellent agreement with the observed one as shown in Fig. 2(a″).

After the purification, the EXAFS oscillation is different from that before the purification. The Fourier transform [Fig. 2(b′)] shows that the Ni-Ni peak at 2.1 Å decreases and a new peak appears around 1.4 Å which may correspond to the coordination of light atoms such as oxygen or carbon. As will be discussed in the XANES section, the peak corresponds to the Ni-C bond and we carry out the curve fitting analyses using carbon atoms: Results are shown in Table II. The coordination number and bond distance are 2.5 and 1.83 Å, respectively. For various Ni-C systems Ni-carbon bond distances are listed in Table III. The Ni-C in the CNF is shorter than Ni-C bonds found in $Ni(cp)_2$ (π bond) and other π bonding compounds. Thus we can rule out the possibility that Ni species form π bonds with carbon atoms in graphene aromatic rings. This means that the Ni-C bond is strongly bound to CNF through σ bond. Since bond lengths for the Ni-C "single bond" are longer than 1.90 Å, the "multiple bond" or some strong specific σ bond as formed in $Ni(CO)_4$ is presumably formed: Actually bond lengths for the Ni-C "double bonds" are in the range of 1.83–1.89 Å, and Ni-C distance is 1.82 Å in $Ni(CO)_4$.

The Ni impurities should occupy substitution site in the graphene sheet or edge site with strong Ni-C bonds. Such strong Ni-C bonds prevent the Ni atoms from being removed by the purification. In addition to the short Ni-C bonds, we find other peak around 2.3 Å, which corresponds to the

TABLE II. Curve fitting results for Ni species in CNF. r is the distance to the neighbor, σ is the Debye-Waller factor, ΔE is a shift in edge energy, R is R-factor defined by Eq. (1).

Sample	Bond	N[a]	r/Å	$\sigma/10^{-2}$ Å	ΔE/eV	R/%	
Before	Ni-Ni	10.8±1.6	2.47±0.02	6.9±3.0	−7±7	1.0	One shell
	Ni-Ni	10.3±1.6	2.47±0.02	6.8±3.0	−7±7		Two shell
	Ni-O	0.8±0.4	2.01±0.03	7.3±3.5	−4±1	0.65	Two shell
After	Ni-C	2.4±0.8	1.83±0.05	6.0±3.0	3±5	5.6	
	Ni-Ni	0.8±0.3	2.48±0.05	5.5±2.0	7±7		

[a]Coordination numbers are corrected by the factor S. $S_{Ni\text{-}Ni}=0.9$ and $S_{Ni\text{-}C}=1.0$ are used.

TABLE III. Ni-C bond length for various Ni-C systems. r is the distance to the neighbor.

Bond type	r/Å	References
Single σ bond	1.90–2.01	56–59
σ bond with aromatic ring	1.90–1.93	60–63
"Double bond"	1.83–1.89	62 and 64
σ bond in metallocycle	1.81–1.91	59, 65, and 66
π bond with "double bond"	2.00–2.21	64, 67, and 68
π bond with "triple bond"	1.87–1.99	69–71
π bond with allyl	1.93–2.11	72 and 68
π with aromatic ring	1.95–2.16	72 and 73
Ni_3C	1.86	39
$Ni(CO)_4$	1.82	74
$Ni(C_5H_5)_2$	2.196	55

Ni-Ni bond distance in Ni foil. Curve fitting analysis shows that the bond distance is 2.48 Å and coordination number is 0.8. In our previous paper,[20] we thought the peak indicated the formation of the Ni dimer in the CNT, but the peak might rather be due to the Ni-Ni bonds in the residual Ni particles because the bond length is quite close to that in Ni foil. This point will be again discussed in the XANES section. Further EXAFS analyses about the location and the detailed structure can be limited because of the one-dimensional information inherent to EXAFS analysis and of the Ni low concentration. Thus we switch our attention to the XANES analysis.

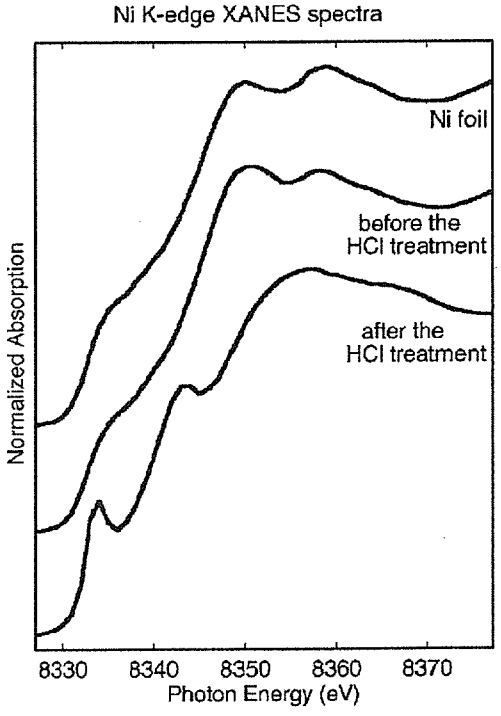

FIG. 3. The observed Ni K-edge XANES spectra of Ni species in the CNF before and after the purification together with that of Ni foil. The experimental data are normalized to the absorption intensity at 8400 eV.

B. XANES

Figure 3 shows the K-edge XANES spectra of Ni species in the CNFs before and after the purification together with that of Ni foil.[20] All the experimental data are normalized to the absorption intensity at 8400 eV, and the calculated atomic absorption cross sections are also normalized in the same way. The XANES spectrum after the purification shows prominent difference from that before the treatment which is quite similar to that for Ni foil. However, the peak at 8350 eV is a little larger than that at 8360 eV. Since $Ni(H_2O)_6(NO_3)_2$ has a peak around 8350 eV, we infer the presence of a small amount of $Ni(H_2O)_6^{2+}$ species. We analyze the observed data on the basis of a regression method using two reference spectra of Ni foil and of $Ni(H_2O)_6(NO_3)_2$ by adjusting the coefficients, c_1 and c_2,

$$\mu_{Ni_{CNF}} = c_1\mu_{foil} + c_2\mu_{Ni(H_2O)_6}, \tag{4}$$

$$c_1 + c_2 = 1, \tag{5}$$

where $\mu_{Ni_{CNF}}$, μ_{foil}, and $\mu_{Ni(H_2O)_6}$ are the Ni K-edge x-ray absorption intensities of Ni species in CNF, of Ni foil and of $Ni(H_2O)_6$. The best fit is obtained when we choose $c_1 = 0.88 \pm 0.05$ as shown in Fig. 4, which supports the presence

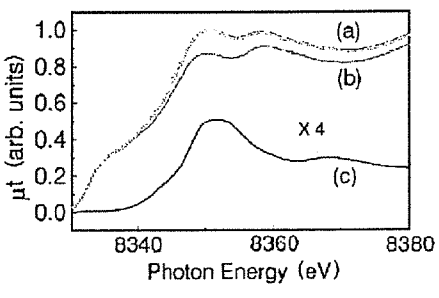

FIG. 4. (Color online) (a) the regression analysis of Ni species in the CNF before the purification. Solid line and circles are observed and best fitted data, respectively. Lines (b) and (c) are the spectra of Ni foil and $Ni(H_2O)_6(NO_3)_2$.

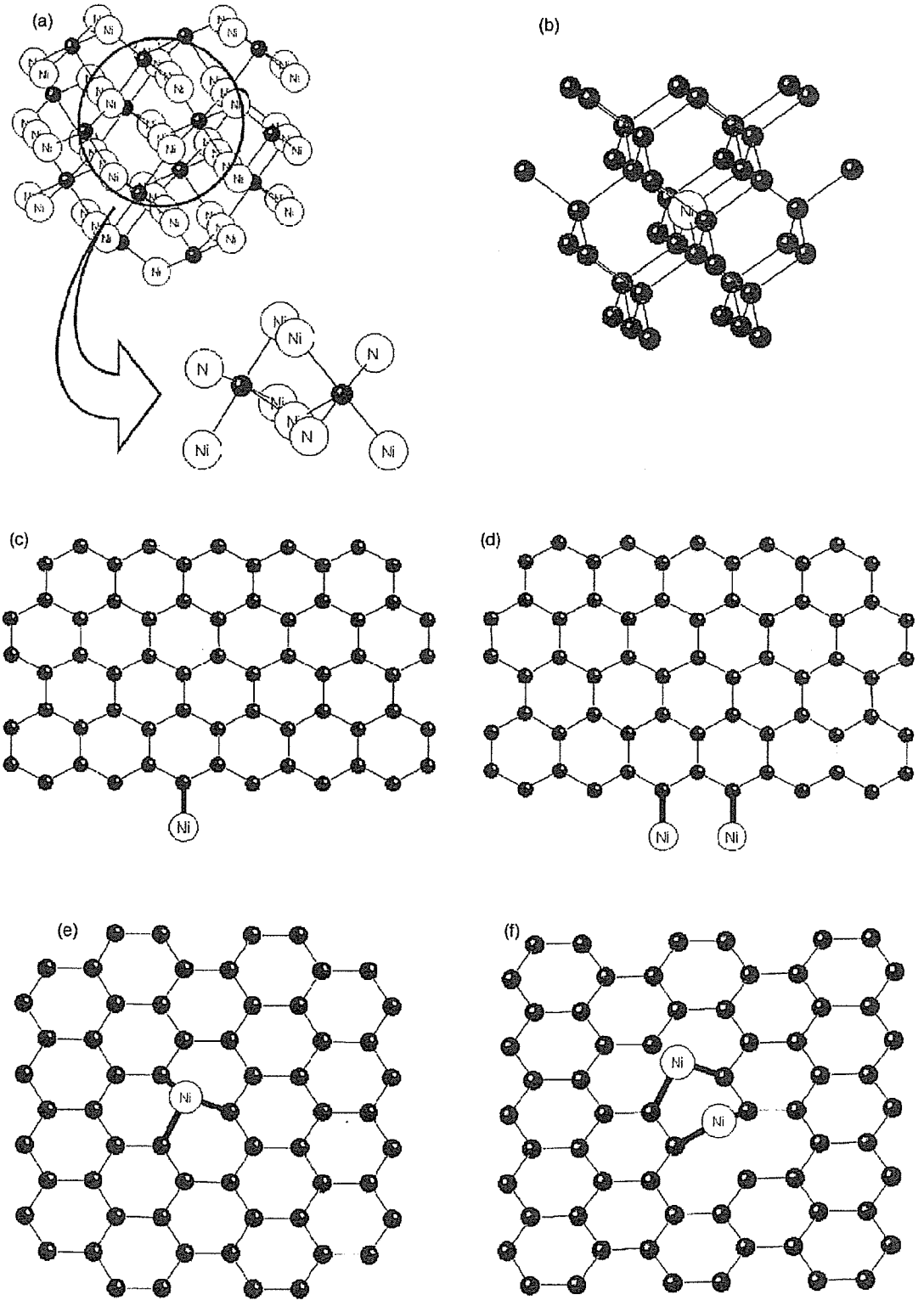

FIG. 5. Local structures of a carbide model (a) and a diamond model (b). In (a) each Ni atom is surrounded by two carbon atoms. In (b) each Ni atom is absorbed in the diamond and surrounded by four carbon atoms. In (c) and (d) edge models, and in (e) and (f) substitution models are shown.

of $Ni(H_2O)_6$ species. This conclusion does not contradict the EXAFS results obtained in the preceding section. The expected coordination number for Ni-Ni and Ni-O based on the c_1 and c_2 are 10.8 ± 0.6 and 0.72 ± 0.04, respectively, which are in good agreement with the estimated ones 10.3 ± 1.6 and 0.8 ± 0.4 by the EXAFS analyses shown in Table II.

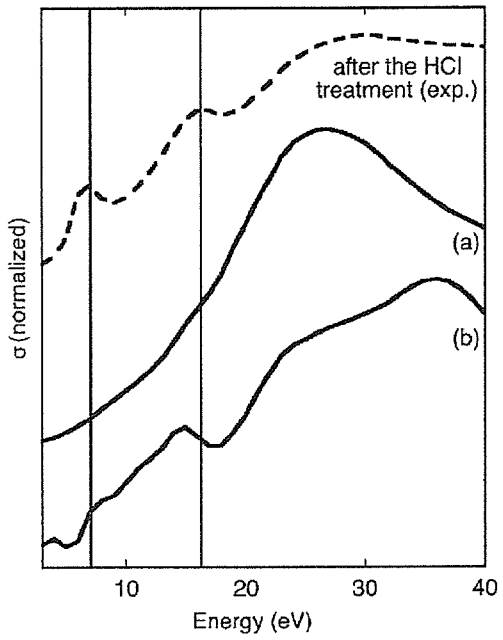

FIG. 6. Calculated XANES spectra for the carbide model (a) and a diamond model (b) shown in Fig. 5 compared with the experimental Ni K-edge XANES after the purification. The energy is measured from the onset of the K-edge absorption.

C. Multiple scattering analysis of XANES

The XANES spectrum after the purification is different from that before the purification. There are two characteristic peaks at the absorption edge regions. This characteristic structure should be the fingerprint for the calculated XANES spectra using multiple scattering theory for several model structures given in Figs. 5 and 9. We investigate the following possible models referring to other experimental findings and theoretical studies:

(1) a carbide model or a diamond model,
(2) an edge model,
(3) a substitution model,
(4) a Stone-Wales defect model.

In these calculations the Ni atoms are assumed to be neutral as supported by our DFT calculations.

1. A carbide model or a diamond model

Although the carbide, Ni_3C contains a quite large number of Ni-Ni pairs (coordination number 12) at 2.63 Å,[39] we consider the carbide model because carbide has often been observed during the catalytic reactions of Ni with CO and hydrocarbons. Figure 6(a) shows the calculated Ni K-edge XANES spectrum for the carbide model shown in Fig. 5(a) compared with the experimental spectrum after the purification. The agreement is quite poor as expected, since no specific peak is observed in the calculated spectrum.

Hayakawa *et al.* have reported micro XANES spectrum for the Ni impurities in the synthetic diamond.[40] They find similar two peaks in the near edge region of the Ni K-edge. The second peak appears at a little higher energy than the corresponding peak in the spectrum of the Ni species in the

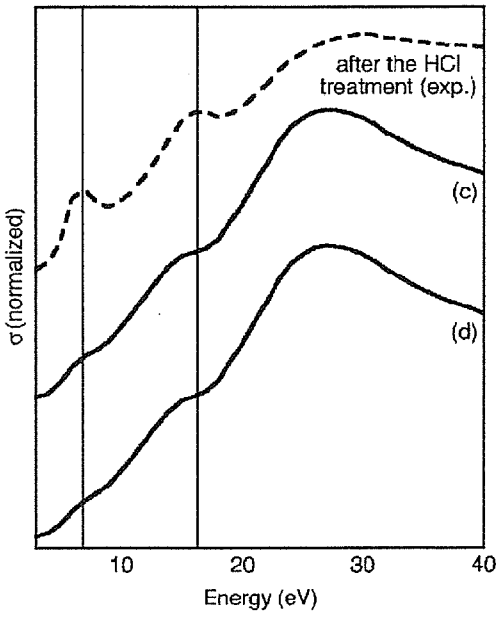

FIG. 7. The calculated XANES spectra for the edge models (c) and (d) shown in Fig. 5 compared with the experimental Ni K-edge XANES after the purification. The energy is measured from the onset of the K-edge absorption.

CNF. They propose a substitution model for the Ni site, i.e., a carbon is replaced by a Ni atom and the replaced Ni is surrounded by four carbon atoms in a tetrahedral symmetry. The model is shown in Fig. 5(b): Ni-C distance is assumed to be 1.8 Å with coordination number 4. The calculated XANES spectrum shown in Fig. 6(b) gives rise to two small peaks. However, the second peak position of the calculated

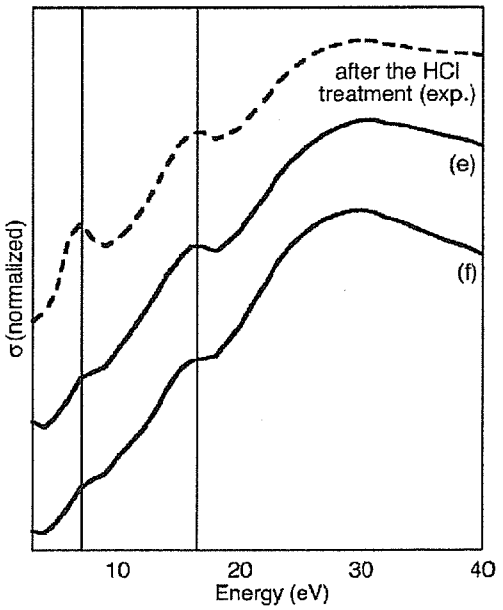

FIG. 8. Calculated Ni K-edge XANES spectra for the substitution models (e) a monomer model and (f) a dimer model compared with the observed spectrum after the purification. The energy is measured from the onset of the K-edge absorption.

XANES spectrum in Fig. 6(b) is different from that of Ni atoms in CNFs measured in this paper. Thus the diamond model is also rejected.

Ni in diamond has been investigated because Ni is a good catalyst for the synthesis of diamond and Ni is efficiently substituted into the diamond to modify the optical and physical properties. Hitherto EPR and theoretical studies have proposed several model structures for Ni impurities in diamond, which support the presence of substitutional Ni.[40,42] However, recent theoretical and ESR results show that the substitutional Ni are not so stable and they are accompanied with defects (one or two vacancies) or impurities (nitrogen).[41,43–46] Further analyses of Ni *K*-edge XANES in diamond should be necessary to confirm their local structures.

2. Edge models

Sharp has discussed the catalytic reaction mechanism for the synthesis of CNT based on the organometallic chemistry.[47] They propose metallocyclic species as an intermediate. At edges of graphene sheets carbon atoms have dangling bonds: Ni atoms can adsorb on the edge of a graphene sheet, forming covalent bonds with C atoms at the edges. We study two different edge models as shown in Figs. 5(c) and 5(d). In both models the Ni-C distance is assumed to be 1.8 Å with coordination number 1. In the latter model Ni dimer structure is assumed with the Ni-Ni distance 2.5 Å. The calculated spectra are shown in Fig. 7. Both models give nearly the same spectra which show quite small shoulders at 7 and 16 eV, and too rapid decrease above 30 eV. These models cannot sufficiently reproduce the observed features.

3. Substitution models

Ni can be on a substitution site in the graphene sheet. Meng *et al.* study the metal-graphene sheet interaction by Hartree-Fock calculations with approximate exchange potential.[13] Their results show strong attractive interaction and bonding with a graphene sheet due to the unfilled 3*d* shell for transition metals. A different theoretical work also supports the substitutional Ni atom in a CNT.[17]

We consider two substitution models—monomer and dimer. In the monomer model as shown in Fig. 5(e), Ni is bound to a graphene sheet through three C-Ni bonds with distance of 1.8 Å. In the dimer model shown in Fig. 5(f), a Ni dimer forms the two C-Ni bonds with the same distance (1.8 Å) and the coordination number 2. In the dimer the Ni-Ni distance is 2.5 Å with coordination number 1. These values are in accordance with the EXAFS results.[20] Figure 8 shows the calculated XANES for the monomer and dimer models shown in Figs. 5(e) and 5(f). We can well reproduce the two characteristic peaks at 7 and 16 eV by the monomer model, although the peak at 7 eV is a little weaker than the observed one. The peak at 7 eV is located just at the beginning of the edge rise and should have a contribution from the atomic bound state that cannot be fully taken into account by the present method. The 16 eV peak is in the continuum character and can successfully be calculated by the multiple scattering theory. The dimer model shows two features at 7 and 16 eV but the peak intensities are one-half of the Ni

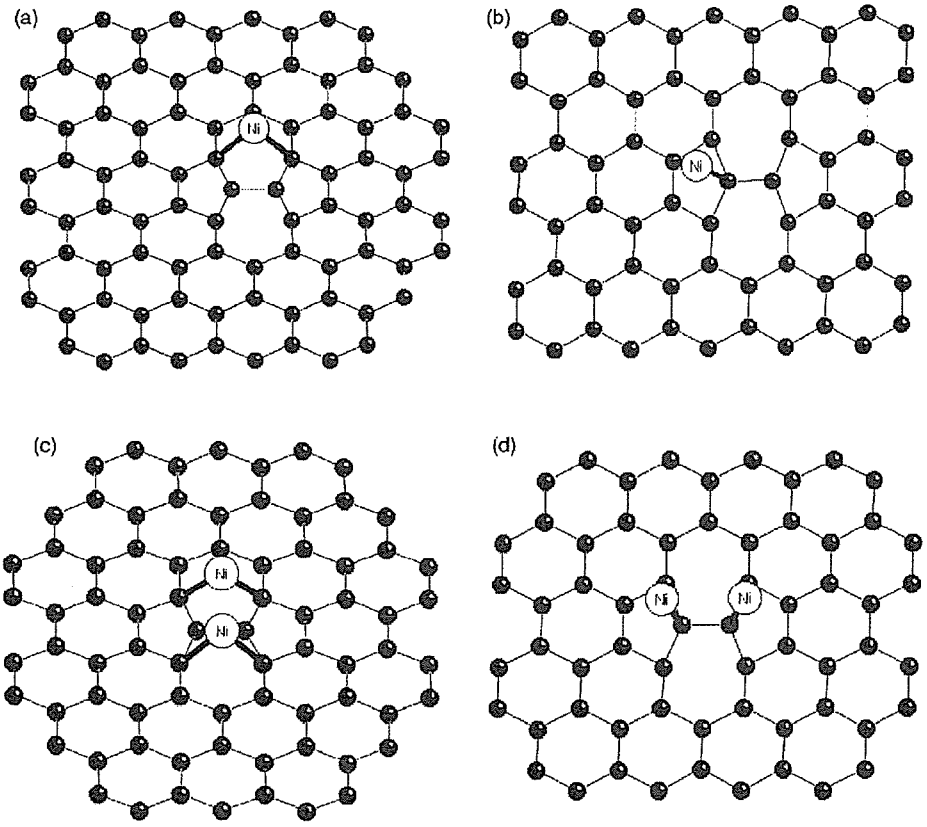

FIG. 9. Four defects models around the Stone-Wales defects. In the model (a) and (b) one Ni atom adsorbs on the 7 and 5 ring, respectively. In model (c) and (d) two Ni atoms adsorb on the 7 and 5 rings, respectively.

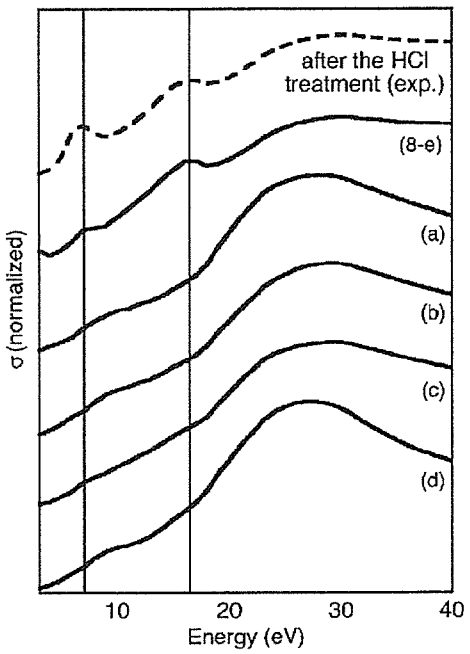

FIG. 10. Calculated Ni *K*-edge XANES spectra for the four models shown in Fig. 9 compared with the experimental spectrum after the purification. For the comparison the calculated spectrum for the model (e) in Fig. 8 is shown as (8-e). The energy is measured from the onset of the *K*-edge absorption.

monomer structure. The structure above 30 eV region is not well fitted to the observed one in the dimer structure. The CNF is composed of multilayer with interlayer distance 3.4 Å.[12,48] We add another sheet (two-sheet model), but we cannot find its remarkable effect on the calculated spectra since the bond length of the Ni-C in the next sheet is quite large.

We thus conclude that most of Ni impurities are in monomer structures in a graphene sheet; each of them substitutes a carbon atom.

4. Stone-Wales defect models

An important defect in the CNT is a Stone-Wales defect where a pair of 5–7 rings can be created by rotating a C-C bond in the hexagonal network by 90°.[49] Recent molecular orbital calculations show that the introduction of Stone-Wales defects would benefit the adsorption capacity of B, N, F, and Si among 10 foreign atoms (H, B, C, N, O, F, Si, P, Li, and Na).[50] This result suggests that the Stone-Wales defects can be the Ni adsorption sites. (See Figs. 9 and 10.) Figure 10 shows the XANES spectra based on the four models shown in Fig. 9. The adsorption models around the Stone-Wales defects (a)–(d) fail to explain the two specific peaks at 7 and 16 eV, and we can rule out the above models.

D. Comparison with literature

In our calculations, the substitution model shown in Fig. 5(e) gives good fit to the observed data. Takenaka *et al.* have also observed the two peaks discussed in this paper in the

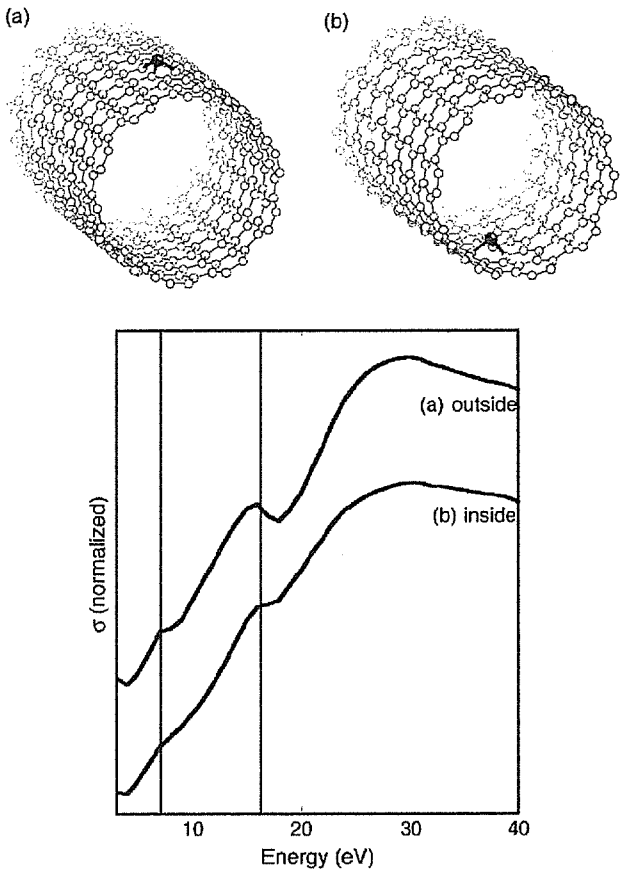

FIG. 11. Two tube models and the calculated XANES spectra. The tube type is armchair which is (10,10) tube with 14 Å in diameter. We assume that Ni atoms are present at the substitution sites whose local adsorption structures are nearly the same as those shown in Fig. 5(e). In model (a) the Ni is located outside of the tube, and in model (b) the Ni is located inside the tube. Calculated Ni *K*-edge XANES spectra are shown for the two tube models.

XANES spectra of the heavily deactivated Ni catalyst after the CH_4 decomposition reaction to carbon filament.[51] They compared the XANES and EXAFS of the "Ni carbide" with those of the known Ni_3C, and found that both spectra were completely different. This result clearly shows that the Ni carbide prepared from the methane decomposition is not the Ni_3C species. They were not able to determine the structure because the strong Ni-Ni peak in Fourier transformed EXAFS spectra for Ni particles were observed at the same time. Judging from the peak positions in the XANES spectra and Fourier transform peaks in the EXAFS, the deactivated Ni they observed should be the same one discussed in this work.

The proposed structure as shown in Fig. 5(e) has already been suggested by Banhart *et al.* in the onionlike graphitic networks.[18] They observe Ni atoms in graphitic carbon onions by TEM and observed a zigzag structure, which indicates the formation of a new C-Ni phase. Their first principle calculations show that the Ni-substituted graphite structure with C-Ni distance 1.8 Å is quite consistent with our XAFS results. Their Car-Pallinello simulation suggests the high stability of this substituted Ni atom in the graphene sheet. Andriotis *et al.* study Ni in a CNT framework using a tight

binding molecular dynamics method.[17] They also find the substitutional Ni in a CNT with Ni-C distance 2.03–2.08 Å: The distances are much longer than our result where Ni-C distance=1.83 Å. Consequently, the Ni substitution model is the most plausible structure of the Ni species which strongly interact with the graphene sheet.

E. XANES application to nanomaterials in combination with multiple scattering analysis

In this work we determine the location and structure of Ni species in the CNF by XAFS and multiple scattering analyses. We also evaluate the sensitivity of XANES to Ni-C distance and Ni charge. We find that we can determine the Ni-C distance within the precision of ±0.1 Å. The distance error bar of XANES is one order bigger than that of EXAFS. Thus the combination of EXAFS and XANES must be necessary. The charge and valence state of metal species can often be inferred from XANES. The edge shift is corresponding to the chemical shift in XPS and the L_2,L_3 white line peaks are related to the density of d vacancy.

We also check how the curvature of the CNT affects the XANES spectra by using multiple scattering theory. We postulate CNTs with 14 Å in diameter as shown in Fig. 11. We set one Ni atom both outside (a) and inside (b) the tube. Comparing the XANES for the Ni on a graphene sheet with the XANES for the Ni outside the CNT with 14 Å, we can see that the curvature has only small influence on the XANES spectra. However, the "inside" model gives much weaker peaks at 7 eV and 16 eV. This may be because the different distances to carbon atoms in next nearest neighbors affect the XANES spectra in these models. This result is quite interesting because any other experimental tools cannot provide such information. Some theoretical simulations support the "outer" models considered here.[14,16,17] The question about the metal location inside or outside of a CNT can be answered based on the XANES analyses.

Thus the XANES in combination with multiple scattering method will provide a new and unique structural tool to study nanomaterials.

F. Comments on the application of CNTs and CNFs prepared from Ni catalysts

Nanotoxicology is a new terminology to evaluate the toxicological hazard to human body and environment.[52] Nanotechnology is revolutionarily developing and is changing our daily life. But the assessment of toxic effects of the nanomaterials is not fully accomplished and nobody knows how the nanomaterials damage ourselves and our environment. One can understand the situation easily in the example of asbestos. Our XAFS analyses that show the presence of strongly bound Ni in a CNF and the facts that Ni is a toxic element suggest that the CNTs and CNFs produced from Ni catalysts should not be used for biomaterials.

V. CONCLUDING REMARKS

In this paper we investigate the local Ni structures before and after the purification of CNFs by EXAFS and XANES. Ni atoms are dominantly in Ni particles together with small amount of Ni oxide before the purification. After the purification they are in Ni monomer species substituted in the graphene sheet to form strong Ni-C bonds.

We have few reliable characterization techniques for small amount of residual species. This work demonstrates the remarkable usefulness of the XAFS (XANES+EXAFS) techniques combined with multiple scattering calculations. In particular XANES can give a detailed stereochemical structures of the Ni species, although it is not so sensitive to the bond distance. In contrast, EXAFS is sensitive to the bond length to nearest neighbors within 0.01 Å. A combination of these two techniques should be a powerful tool for the studies of nanosciences.

ACKNOWLEDGMENTS

The authors are grateful to K. Kaneko, H. Kano, S. Nagamatsu, Y. Hattori, and K. Ohminami for their valuable comments on this work. The work was financially supported by "A new EXPEEM," Grant No. 20702026 of JST, the Grant-in-Aid for Scientific Research, Category S (Grant No. 16106010) of JSPS (Japan Society for Promotion of Science), and Health and Labour Sciences Research Grants in Research on Advanced Medical Technology from the Ministry of Health, Labour and Welfare. The EXAFS measurements were carried out under the approval of the Photon Factory Advisory Committee (PAC Approval number 99G280 2001G117 and 2003G247).

*Electronic address: tfujikawa@faculty.chiba-u.jp

[1] S. Iijima, Nature (London) **354**, 56 (1991).
[2] S. Iijima and T. Ichihashi, Nature (London) **63**, 603 (1993).
[3] N. M. Rodriguez, A. Chambers, and R. T. K. Baker, Langmuir **11**, 3862 (1995).
[4] M. Endo, Y. A. Kim, T. Hayashi, Y. Fukai, K. Oshida, M. Terrones, T. Yanagisawa, S. Higaki, and M. S. Dresselhaus, Appl. Phys. Lett. **80**, 1267 (2002).
[5] K. Tohji, H. Takahashi, Y. Shinoda, N. Shimizu, B. Jeyadevan, I. Matsuoka, Y. Saito, A. Kasuya, S. Ito, and Y. Nishina, J. Phys. Chem. B **101**, 1974 (1997).
[6] E. Dujardin, C. Meny, P. Panissod, J.-P. Kintzinger, N. Yao, and T. W. Ebbesen, Solid State Commun. **114**, 543 (2000).
[7] L. Grigorian, G. U. Sumanasekera, A. L. Loper, S. L. Fang, J. L. Allen, and P. C. Eklund, Phys. Rev. B **60**, R11309 (1999).
[8] H. J. Choi, J. Ihm, S. G. Louie, and M. L. Cohen, Phys. Rev. Lett. **84**, 2917 (2000).
[9] A. N. Andriotis, M. Menon, and G. E. Froudakis, Phys. Rev. B **61**, R13393 (2000).
[10] A. Bianco and M. Prato, Adv. Mater. (Weinheim, Ger.) **15**, 1765 (2003).
[11] G. A. Hughes, Nanomedicine: Nanotechnology, Biology and

Medicine **1**, 22 (2005).
[12] Y. Sato, K. Shibata, H. Kataoka, S. Ogino, F. Bunshi, A. Yokoyama, K. Tamura, T. Akasaka, M. Uo, K. Motomiya, B. Jeyadevan, R. Hatakeyama, W. Fumio, and K. Tohji, Mol. BioSyst. **1**, 142 (2005).
[13] F. Y. Meng, L. G. Zhou, S. Q. Shi, and R. Yang, Carbon **41**, 2023 (2002).
[14] Y. Yagi, T. M. Briere, M. H. F. Sluiter, V. Kumar, A. A. Farajian, and Y. Kawazoe, Phys. Rev. B **69**, 075414 (2004).
[15] A. Andriotis, M. Menon, and G. Froudakis, Appl. Phys. Lett. **76**, 3890 (2000).
[16] E. Durgun, S. Dag, V. M. K. Bagci, O. Gülseren, T. Yildirim, and S. Ciraci, Phys. Rev. B **67**, 201401(R) (2003).
[17] A. N. Andriotis, M. Menon, and G. Froudakis, Phys. Rev. Lett. **85**, 3193 (2000).
[18] F. Banhart, J. C. Charlier, and P. M. Ajayan, Phys. Rev. Lett. **84**, 686 (2000).
[19] Y. H. Lee, S. G. Kim, and D. Tomanek, Phys. Rev. Lett. **78**, 2393 (1997).
[20] K. Asakura, W. J. Chun, K. Tohji, Y. Sato, and F. Watari, Chem. Lett. **34**, 382 (2005).
[21] J. J. Rehr and R. C. Albers, Rev. Mod. Phys. **72**, 621 (2000).
[22] K. Uno, Y. Notoya, T. Fujikawa, H. Yoshikawa, and K. Nishikawa, Jpn. J. Appl. Phys., Part 1 **44**, 4073 (2005).
[23] T. Fujikawa, J. Phys. Soc. Jpn. **62**, 2155 (1993).
[24] S. Nagamatsu, N. Ichikuni, S. Shimazu, T. Fujikawa, K. Fukuda, and T. Uematsu, Phys. Scr., T **T115**, 756 (2005).
[25] Y. Notoya, K. Hayakawa, T. Fujikawa, T. Kubota, T. Shiodo, K. Asakura, and Y. Iwasawa, Chem. Phys. Lett. **357**, 365 (2002).
[26] K. Asakura, T. Kubota, W. J. Chun, Y. Iwasawa, K. Ohtani, and T. Fujikawa, J. Synchrotron Radiat. **6**, 439 (1999).
[27] K. Ohtani, T. Fujikawa, T. Kubota, K. Asakura, and Y. Iwasawa, Jpn. J. Appl. Phys., Part 1 **36**, 6504 (1997).
[28] K. Ohtani, T. Fujikawa, T. Kubota, K. Asakura, and Y. Iwasawa, Jpn. J. Appl. Phys., Part 1 **37**, 4134 (1998).
[29] N. M. Rodriguez, J. Mater. Res. **8**, 3233 (1993).
[30] M. Nomura and A. Koyama, Nucl. Instrum. Methods Phys. Res. A **467**, 733 (2001).
[31] M. Nomura and A. Koyama, J. Synchrotron Radiat. **6**, 182 (1999).
[32] K. Asakura, in *X-ray Absorption Fine Structure for Catalysts and Surfaces*, edited by Y. Iwasawa (Singapore, Singapore, 1996), p. 33.
[33] T. Taguchi, T. Ozawa, and H. Yashiro, Phys. Scr., T **T115**, 205 (2005).
[34] T. Fujikawa, T. Matsuura, and H. Kuroda, J. Phys. Soc. Jpn. **52**, 905 (1983).
[35] T. Fujikawa and N. Yiwata, Surf. Sci. **357**, 60 (1996).
[36] T. Fujikawa, R. Yanagisawa, N. Yiwata, and K. Ohtani, J. Phys. Soc. Jpn. **66**, 257 (1997).
[37] T. Fujikawa, K. Nakamura, S. Nagamatsu, and J. J. Rehr, J. Phys. Soc. Jpn. **71**, 357 (2002).
[38] R. B. Greegor and F. W. Lytle, J. Catal. **63**, 476 (1980).
[39] S. Nagakura, J. Phys. Soc. Jpn. **13**, 1005 (1958).
[40] S. Hayakawa, F. Nakamura, Y. Goshi, M. Wakatsuki, and H. Kaji, Trans. Mater. Res. Soc. Jpn. **14B**, 1559 (1994).
[41] J. P. Goss, P. R. Briddon, R. Jones, and S. Oberg, J. Phys.: Condens. Matter **16**, 4567 (2004).
[42] J. Isoya, H. Kanda, J. R. Norris, J. Tang, and M. K. Bowman, Phys. Rev. B **41**, 3905 (1990).
[43] J. E. Lowther, Phys. Rev. B **51**, 91 (1995).
[44] K. Iakoubovskii, A. Stesmans, B. Nouwen, and G. J. Adriaenssens, Phys. Rev. B **62**, 16587 (2000).
[45] K. Iakoubovskii, Phys. Rev. B **70**, 205211 (2004).
[46] K. Iakoubovskii and A. T. Collins, J. Phys.: Condens. Matter **16**, 6897 (2004).
[47] P. R. Sharp, J. Organomet. Chem. **683**, 288 (2003).
[48] S. Reich, C. Thomsen, and J. Maultzsch, *Carbon Nanotube. Basic Concepts and Physical Properties* (Wiley-VCH, New York, 2004).
[49] A. J. Stone and D. J. Wales, Chem. Phys. Lett. **128**, 501 (1986).
[50] L. G. Zhou and S. Q. Shi, Carbon **41**, 579 (2003).
[51] S. Takenaka, H. Ogihara, and K. Otsuka, J. Catal. **208**, 54 (2002).
[52] R. F. Service, Science **304**, 1732 (2004).
[53] S. Sasaki, K. Fujino, and Y. Takeuchi, Proc. Jpn. Acad., Ser. A: Math. Sci. **55**, 43 (1979).
[54] F. Bigoli, A. Brainbanti, A. Tiripicchio, and M. Tiripicchi-Camellini, Acta Crystallogr., Sect. B: Struct. Crystallogr. Cryst. Chem. **24**, 1982 (1968).
[55] L. Hedberg and K. Hedberg, J. Chem. Phys. **53**, 1228 (1970).
[56] K. R. Poerschke, K. Jonas, G. Wilke, R. Benn, R. Mynott, R. Goddard, and C. Krueger, Chem. Ber. **118**, 275 (1985).
[57] W. Kaschube, K. R. Porschke, K. Angermund, C. Kruger, and G. Wilke, Chem. Ber. **121**, 1921 (1988).
[58] H.-F. Klein, T. Weimer, M. J. Menu, M. Dartiguenave, and Y. Dartiguenave, Inorg. Chim. Acta **154**, 21 (1988).
[59] J. Langer, R. Fischer, H. Gorls, and D. Walther, J. Organomet. Chem. **689**, 2952 (2004).
[60] M. W. Eyring and L. J. Radonovich, Organometallics **4**, 1841 (1985).
[61] M. M. Brezinski, J. Schneider, L. J. Radonovich, and K. J. Klabunde, Inorg. Chem. **28**, 2414 (1989).
[62] K. Miki, H. Taniguchi, Y. Kai, N. Kasai, K. Nishiwaki, and M. Wada, J. Chem. Soc., Chem. Commun. **1982**, 1178 (1982).
[63] U. Klabunde, T. H. Tulip, D. C. Roe, and S. D. Ittel, J. Organomet. Chem. **334**, 141 (1987).
[64] B. Gabor, C. Kruger, B. Markzinke, R. Mynott, and G. Wilke, Angew. Chem., Int. Ed. Engl. **30**, 1666 (1991).
[65] P. Buchalski, A. Pietrzykowski, S. Pasynkeiwicz, and L. B. LJerzykeiwicz, J. Organomet. Chem. **690**, 1523 (2005).
[66] D. M. Grove, G. Van Koten, H. J. C. Ubbels, and R. Zoet, Organometallics **3**, 1003 (1984).
[67] H. Maciejewski, A. Sydor, and M. Kubicki, J. Organomet. Chem. **689**, 3075 (2004).
[68] R. Taube, S. Wache, J. Sieler, and R. Kempe, J. Organomet. Chem. **456**, 131 (1993).
[69] K. R. Porschke, R. Mynott, K. Angernand, and C. Kruger, Z. Naturforsch. B **40**, 199 (1985).
[70] M. A. Bennett, J. A. Johnson, and A. C. Willis, Organometallics **15**, 68 (1996).
[71] J. D. Ferrara, C. Tessier-Youngs, and W. J. Youngs, J. Am. Chem. Soc. **107**, 6719 (1985).
[72] R. Appel, F. Knoch, and V. Winkhaus, J. Organomet. Chem. **307**, 93 (1986).
[73] R. M. Pirzer, J. D. Goddard, and H. F. Schaefer, J. Am. Chem. Soc. **103**, 5681 (1981).
[74] D. Braga, F. Grepioni, and A. G. Orpen, Organometallics **12**, 1481 (1993).

Dynamic and static hydrogen effects on mechanical properties in Vanadium alloys

S. Ohnuki, T. Yasuda, K. Yashiki, T. Suda, S. Watanabe

Graduate School of Engineering, Hokkaido University, N-13, W-8, Kita-ku, Sapporo 060-8628, Japan

Abstract. To understand hydrogen behavior in V and V-based alloys, two kinds of tensile tests were carried out for hydrogen-charged miniature specimens: One is with hydrogen charging prior to testing (static charging), and the other is with hydrogen charging during straining (dynamic charging) with the continuous and intermittent ways. *Static hydrogen-charging effect:* From the results of gas emission and microstructure, it was indicated that hydrogen can be trapped by lattice defects, dislocations, vacancies and voids, which were effective up to 500 C. The static charging prior to straining generally resulted in hydrogen-induced hardening. *Dynamic hydrogen-charging effect:* The deformation stress dropped just after starting the dynamic charging, and returned to the original level after stopping the charging, which can be called as a hydrogen-induced softening. The significant softening is attributed to fast diffusion and interactions of hydrogen with mobile dislocations. The activation volume from different strain rate experiment was decreased with hydrogen charging, which means that a small amount of hydrogen can reduce Piers potential for mobile dislocations.

Keywords: Hydrogen, Vanadium alloys, dislocations, Embrittlement, trapping, trapping

INTRODUCTION

Vanadium alloys have extremely high solubility for hydrogen, and are now being considered for commercial hydrogen storage materials and for other uses [1-2]. For example, V-Cr-Ti alloys have been a candidate material for core components in fusion energy systems, because of high temperature strength and good radiological properties. Because of absorption easily from the environment of plasma and liquid coolants, the hydrogen accumulation, as well as gaseous transmutation during neutron irradiation [1-4], is an important factor for determining the lifetime and safety of structural materials. From those factors, hydrogen and its isotopes can easily accumulate and thus influence the mechanical properties and related microstructures [3-4]. Therefore, it is important to understand basics of the hydrogen behavior and the mechanisms involved in microstructural changes.

The objective of this study is to clarify the behavior of hydrogen in vanadium based alloys, particularly from the point of view of mechanical properties and microstructure, which could aid in the development of advanced vanadium alloys.

EXPERIMENTAL PROCEDURES

The specimens of vanadium and V-4Vr-4Ti alloy were provided by the National Institute for Fusion Science (NIFS) and chemical composition is included in the reference [5]. The specimens were cold-rolled to a thickness of 0.25mm and annealed at 900℃ for 1 hour, where the grain size was approximately 50 micron. Some amount

CP837, *Hydrogen in Matter: Second International Symposium on Hydrogen in Matter (ISOHIM)*,
edited by G. R. Myneni and B. Hjörvarsson

of V-4Ti and V-4Cr alloys were used for this experiment. Neutron irradiation was carried out in JMTR to a damage dose of about 0.01 dpa (1 x 10^{19} n/cm^2) at 290 C.

Hydrogen charging was conducted using two techniques 1) static hydrogen charging prior to tensile testing, and 2) dynamic charging during tensile testing. Static hydrogen charging was performed by electrolysis in 1N-H_2SO_4 at a current density of about 6.7 mA/cm^2, for example. Figure 1 shows the apparatus for this experiment. Dynamic charging was performed during the straining, and was initiated as soon as yielding occurred. Two modes were used for the dynamic charging. In the intermittent method, the charging was conducted for 5 seconds at each 5% increase in the strain. In the continuous method, the charging was continued until eventual failure. In order to change the dissolved hydrogen level during the dynamic charging, the concentration of the H_2SO_4 solution was varied between 0.5 and 1.0 N and the current density was varied between 7 and 33 mA/cm^2. The details of the charging have been reported [6].

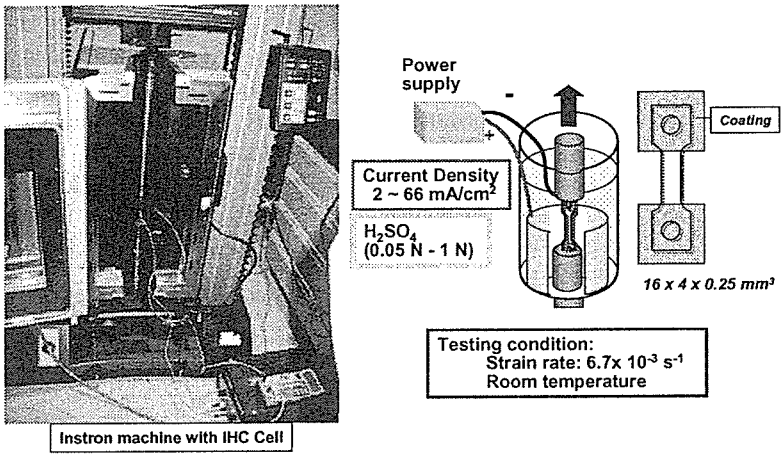

FIGURE 1. Illustration of apparatus for dynamic charging experiments, combined with conventional Instron machine. The apparatus was used for static charging experiment.

RESULTS AND DISCUSSION

Hydrogen-induced hardening in irradiated vanadium alloy

Figure 2 shows the yield stress as a function of static charging time in V-4Cr alloy for comparing with un-irradiated and irradiated to 0.01 dpa at 290 C in JMTR. In the un-irradiated material, yield stress showed slight decreasing in at short charging time (< 300 s) followed by slight increasing at long charging time. The overall increase of about 30 MPa is attributed to solution hardening. In the irradiated sample, the neutron irradiation caused a significant increase in the yields stress of 250 MPa. Hydrogen charging resulted in an additional increase of up to 150 MPa, which was essentially proportional to the charging time.

Figure 3 shows hydrogen emission profile from neutron irradiated and H-charged V, where the tailing was observed at high temperature side and suggested the several types of trappings. After comparing with un-irradiated and irradiated materials, including microstructures, it is assumed that the profile can be decomposed to four

peaks; peak 1 at 375 C is assumed for interstitial H, peak 2 at 420C is for dislocation trapping, peak 3 at 480 C is for vacancy trapping, and peak 4 at 530 C is for void trapping. It is sure that hydrogen can be trapped by irradiation-produced defects, and is stable up to about 500 C [6]. For explaining the additional hardening due to hydrogen charging, the interaction between defect clusters and hydrogen should be main factor.

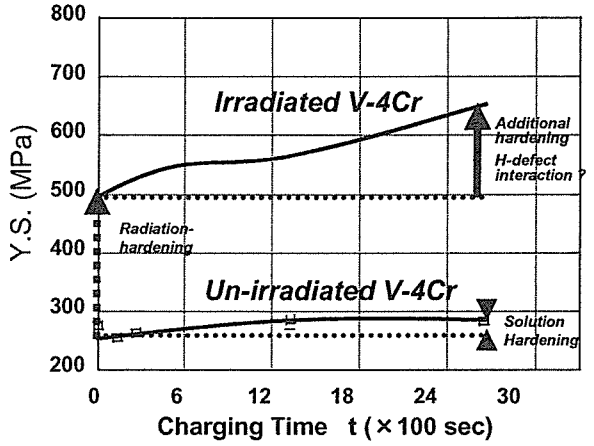

FIGURE 2. Yield stress as a function of static charging time in V-4Cr alloy neutron-irradiated to $1x10^{19}$ n/cm^2 at 290 C in JMTR.

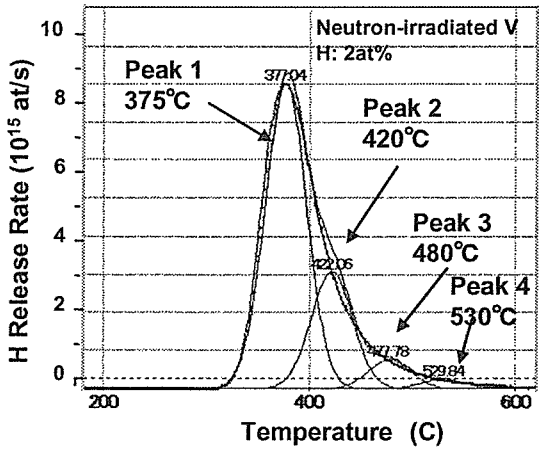

FIGURE 3. Hydrogen emission as a function of temperature for neutron irradiated and H-charged V sample, which was decomposed to four peaks.

Dynamic charging effect on mechanical properties

Figure 4 shows the stress-strain curves during dynamic charging with interval for V and V-4Cr-4Ti at different charging current levels. Both samples showed softening and hardening relative to the current, that is similar as reported [8]. Therefore, hydrogen-induced softening and hardening can be seen as general phenomena in V and V based alloys. Figure 5 shows enlarged parts of the stress-strain curves for different charging conditions with the interval of 5 second charging. As is evident, there was a clear response in the stress curve at both the beginning and the end of the charging. At low H levels, the stress dropped quickly at the start of the cycle, followed by a somewhat slower asymptotic return to the original level at the end of the cycle. At

high H levels, however, the decrease in stress was smaller and somewhat slower at the start of the cycle, followed by an overall increase in the stress at the end of the cycle which was higher than in V. These results indicate that this transient phenomenon based on competitive process of softening and hardening during charging.

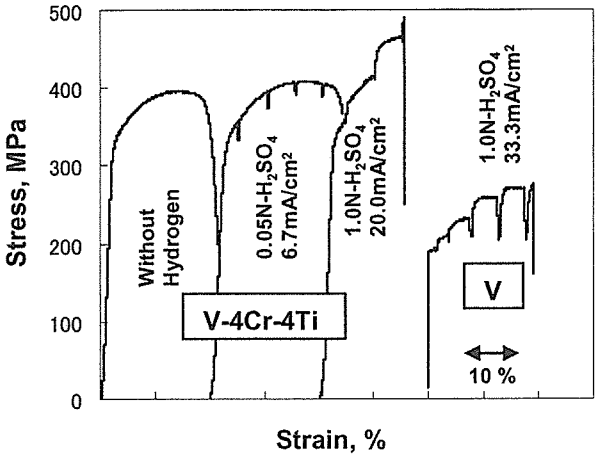

FIGURE 4. Stress-strain curves during dynamic charging with interval for V and V-4Cr-4Ti. Both samples showed softening and hardening behavior relative to the current.

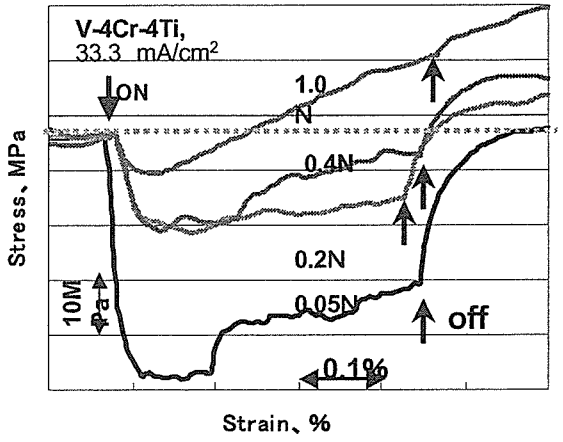

FIGURE 5. Dynamic charging during tensile testing of V-4Cr-4Ti. The Stress responded rapidly to the on and off of the current (interval charging). At low H levels, fast response and significant stress decrease (softening) are confirmed, which then recovers to its original level. At high H levels, a smaller loss of stress is seen, followed by an overall increase in the hardening.

Mechanism for hydrogen-induced softening and hardening

Figure 6 shows a typical stress-strain curve for dynamic charged V after reaching the yield point. The charging was performed carefully at 6.7 mA/cm^2 in a solution of 1N-H_2SO_4. Two stages were observed during continuous dynamic charging. (a) is the microstructure corresponded to the end of the first stage, where only tangled dislocations are observed, and (b) is the microstructure from the end of the second

stage, where plate-like hydrides and dislocation with high density were developed. The arrows indicate hydride platelets and extra spots in the electron diffraction (V_2H). In this condition, the hydride formation was delayed as compared with the static charging. Figure 7 shows the relation between analyzed hydrogen contents in V and static and dynamic charging times. In the static charging, the content increased with the square root of the static charging time, which means this process should be controlled by the H diffusion. From TEM observations, hydride formation was confirmed above 0.2 wt %; therefore, the solubility limit is about 0.2 wt % at room temperature. In the case of dynamic charging, the analyzed hydrogen content was quite low as comparing to static charging. The difference of 0.3 wt%, as indicated by arrow, can be caused by the effects of generated and moved dislocations. This suggests that interactions between the hydrogen and the dislocations resulted in significant hydrogen emission during the dynamic charging.

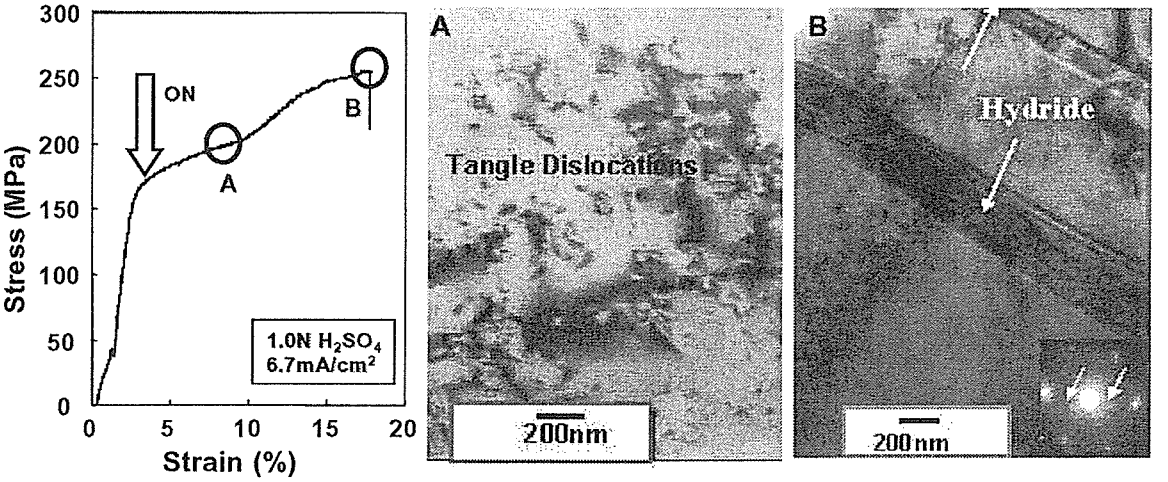

FIGURE 6. Two stages developed during continuous dynamic charging, which correspond to different microstructures; (a) only tangled dislocations, and (b) hydride plates and dislocations with high density, where the hydride formation was delayed as compared to static charging.

The actual mechanisms for hydrogen induced softening and hardening has not been completely understood, but it can be explained that Piels potential is changed by the trapped hydrogen which may diffuse quickly even at room temperature. Recently, authors examined the activation volume for deformation under dynamic H-charging with changing the strain rate in the range of $10^{-3} - 10^{-4}$ at each temperature [9]. The volume showed increasing tendency with increasing test temperature, but H-charging made the reduction of the activation volume with aout 10 % at the temperature range of 230 – 300 K.

Figure 8 shows a schematic illustration of the dynamic interaction between the hydrogen and the dislocations that can explain the softening, hardening and gas emission. At low hydrogen concentration, (a) the dislocation mobility should be enhanced due to the H atmosphere, (b) the gliding of dislocation with H induces gas